Supporting Information

Achieving active and durable oxygen reduction/evolution reactions on protonic ceramic electrochemical cells with spinel-based air electrodes

*Wanqing Deng, Yangsen Xu, Xirui Zhang, Jiaojiao Xia, Kang Xu, Hui Gao, Yu Chen**

School of Environment and Energy, State Key Laboratory of Luminescent Materials and Devices, Guangdong Provincial Key Laboratory of Atmospheric Environment and Pollution Control, South China University of Technology, Guangzhou 510006, China

**Corresponding author: Yu Chen (E-mail: eschenyu@scut.edu.cn)*

Supplementary Note 1:

The proton conductivity of $BaZr_{0.8}Y_{0.2}O_{3-\delta}$ (BZY) has been reported by several groups to be higher than 0.01 S cm^{-1} at temperatures between 450 and 500°C.[1, 2] An air electrode with high electrocatalytic activity towards oxygen reduction and oxygen evolution reactions is related to its excellent triple conductivity of $H^+/O^{2-}/e^-$.[3] The addition of BZY was expected to increase the proton conductivity and enlarge the three-phase interface of the composite air electrode to enhance the electrocatalytic activity towards the oxygen reduction and oxygen evolution reactions. In addition, the thermal expansion coefficient of BZY is 9.55×10^{-6} K^{-1},[3] which matches well with MCCO. The coupled BZY with MCCO could optimize the thermal compatibility between the air electrode and the electrolyte.

Supplementary Note 2:

MCCO-BZY and MCO-BZY inks were brushed-painted on the dense BZCYYb electrolyte surface and co-sintered at 900^{o}C in the air for 10 min to form the single cells, in which no sintering additives were used. One of the main purposes of the single cell being fired at 900^{o}C is to remove the carbonaceous organic material (such as terpinol and ethyl cellulose) to form the porous structure. Besides, the thermal expansion coefficient (TEC) of the MCCO is 9.0×10^{-6} K^{-1} from room temperature to 300^{o}C, and 15.0×10^{-6} K^{-1} from 300^{o}C to 1000^{o}C. The TEC value of MCCO is closer to that of the proton-conducting electrolyte BZCYYb used in this study, which is 9.8×10^{-6} K^{-1}.[4] The similar thermal compatibility was beneficial for short-term single-cell operation and cycling tests. In addition, the thermal expansion coefficient of BZY is 9.55×10^{-6} K^{-1}.[5] The coupled BZY with MCCO could optimize the thermal compatibility between the air electrode and the electrolyte. **Figure 3a** shows the scanning electron microscopy (SEM) images of the MCCO-BZY single cell after the durability tests. It is shown that the air electrode has a porous structure, which is beneficial for mass diffusion and transport. There are no apparent cracks in the tri-layer structure.

Supplementary Note 3:

In the electrolysis mode, H_2O is transported to the air electrode side. In the presence of the applied voltage, H_2O is decomposed into O_2 and protons:

$$\text{Air electrode: } H_2O \rightarrow 2H^+ + O_2 + 2e^-.$$

Then, the protons migrate through the dense BZCYYb electrolyte, while the electrons are conveyed through an external circuit to the fuel electrode, eventually producing dry H_2:

$$\text{Fuel electrode: } 2H^+ + 2e^- \rightarrow H_2.$$

Gas chromatography (GC, GC-7820) was used to examine the H_2 concentration on the fuel electrode side to evaluate the Faradic efficiencies of the air electrodes in the electrolysis mode, which was obtained according to the ratio of the amount of H_2 produced in the experiment with a fixed current density to its theoretical value. Displayed in **Figure S22** is the schematic illustration of the water-splitting on the MCCO-BZY air electrode surface in the protonic ceramic electrochemical cells.

Table S1. The XPS analysis of oxygen species for MCO powder

MCO	Position (eV)	Area	$(O^-/O_2^{2-})/O^{2-}$
H_2O/CO_3^{2-}	533.36	13508.51	0.3672
O_2/OH^-	531.83	56997.13	
O_2^{2-}/O^-	530.65	40096.06	
O^{2-}	529.98	109186.10	

Table S2. The XPS analysis of oxygen species for MCCO powder

MCCO	Position (eV)	Area	$(O^-/O_2^{2-})/O^{2-}$
H_2O/CO_3^{2-}	533.36	16873.28	0.5929
O_2/OH^-	531.83	57506.85	
O_2^{2-}/O^-	530.66	60622.42	
O^{2-}	529.87	102249.50	

Table S3. The XPS analysis of Co $2p_{3/2}$ for MCO powder

MCO	Position (eV)	Area	Content
Co^{2+}	778.77, 793.83	50338.60	28%
Co^{3+}	779.24, 794.97	78180.84	43%
Co^{4+}	780.64, 796.23	52638.37	29%

Table S4. The XPS analysis of Co $2p_{3/2}$ for MCCO powder

MCCO	Position (eV)	Area	Content
Co^{2+}	778.64, 793.75	43116.16	19%
Co^{3+}	779.23, 794.66	86491.78	37%
Co^{4+}	780.56, 795.72	102365.99	44%

Table S5. The XPS analysis of Mn 2p for MCO powder

MCO	Position (eV)	Area	Content
Mn^{2+}	640.02	39695.18	22%
Mn^{3+}	641.61, 651.90	83071.14	45%
Mn^{4+}	643.71, 653.40	59961.91	33%

Table S6. The XPS analysis of Mn 2p for MCCO powder

MCCO	Position (eV)	Area	Content
Mn^{2+}	640.02	39695.18	22%
Mn^{3+}	641.61, 651.90	83071.14	45%
Mn^{4+}	643.71, 653.40	59961.91	33%

Table S7. Temperature dependence of the polarization resistance (R_p) of symmetrical cells with MCCO-BZY and other high-performance electrodes reported recently.

Air electrode	Electrolyte	Temp. [^oC]	R_p [Ω cm^2]	Authors, Year
MCO-BZY	BZCYYb	700	0.133	This work
		650	0.299	
		600	0.704	
		550	2.222	
		500	8.543	
MCCO-BZY	BZCYYb	700	0.107	This work
		650	0.217	
		600	0.418	
		550	1.076	
		500	3.190	
MCCO-ScSZ	ScSZ	800	0.03	Thanheem et al. 2019[6]
		750	0.06	
		700	0.2	
		650	0.57	
CBO-GDC	YSZ	700	0.58	Li et al. 2021[7]
		650	1.62	
		600	5.59	
		550	14.87	
CMO	ScSZ	800	0.14	Zhen et al. 2016[8]
		750	0.32	
		700	0.66	
		650	1.47	
MCO-YSZ	YSZ	800	0.43	Liu et al. 2013[9]

		700	＞2	
		650	＞4	
NFCO	SDC	700	0.73	Rao et al. 2013[10]
		650	1.51	
		600	3.95	
CFO	LSGM	800	0.37	Cui et al. 2019[11]
		750	0.58	
		700	1.06	

Table S8. Temperature dependence of the PPDs of single cells with MCCO-BZY and other high-performance electrodes reported recently.

Air electrode	Electrolyte	Fuel electrode	Temp. [^{o}C]	P_{max} [W cm^{-2}]	Authors, Year
MCO-BZY	BZCYYb	NiO-BZCYYb	700	1.18	This work
			650	0.77	
			600	0.45	
			550	0.26	
			500	0.14	
MCCO-BZY	BZCYYb	NiO-BZCYYb	700	1.81	This work
			650	1.34	
			600	0.86	
			550	0.50	
			500	0.27	
MCO	YSZ	Ni-YSZ	800	0.39	Liu et al. 2011[12]
			750	0.25	
			700	0.14	
			650	0.06	
MCO-SDC	YSZ	Ni-YSZ	800	0.15	Liu et al. 2011[12]
			750	0.13	
			700	0.08	
			650	0.04	
CCO	SSZ	Ni-SSZ	800	0.53	Shao et al. 2016[13]
			750	0.38	
			700	0.29	

CMO	ScSZ	Ni-ScSZ	800	1.08	Zhen et al. 2016[8]
			750	0.81	
			700	0.51	
			650	0.30	
CMCO	YSZ	Ni-YSZ	800	0.50	Liu et al. 2013[9]
			750	0.47	
			700	0.34	
MCCO-ScSZ	ScSZ	NiO-YSZ	800	1.92	Thanheem et al. 2019[6]
			750	1.74	
			700	1.38	
FMCNZ-GDC	YSZ	NiO-YSZ	800	1.08	Xu et al. 2022[14]
			750	0.92	
			700	0.75	
			650	0.55	
ZCO	BZCY	NiO-BZCY	700	1.60	Xu et al. 2022[15]
			650	1.24	
			600	0.82	
CFLO	BZCY	NiO-BZCY	700	1.05	Yang et al. 2022[16]
			650	0.75	
			600	0.50	
			550	0.30	

Table S9. Temperature dependence of the current density at 1.3V of single cells with MCCO-BZY and other high-performance electrodes reported recently.

Air electrode	Electrolyte	Fuel electrode	Temp. [°C]	Current density @1.3V [A cm^{-2}]	Authors, Year
MCO-BZY	BZCYYb	NiO-BZCYYb	700	-3.13	This work
			650	-1.75	
			600	-0.97	
			550	-0.51	
			500	-0.24	
MCCO-BZY	BZCYYb	NiO-BZCYYb	700	-3.57	This work
			650	-2.29	
			600	-1.17	
			550	-0.55	
			500	-0.21	
NBSCF-BZCYYb	BZCYYb	Ni-BZCYYb	750	-3.16	Kim et al. 2018[17]
			700	-2.41	
			650	-1.62	
			600	-0.75	
LSN	BCZY	Ni-BCZY	700	-1.37	Yang et al. 2018[18]
			600	-0.42	
PBCC	BZCYYb	Ni-BZCYYb	600	-0.72	Tang et al. 2020[19]
			550	-0.39	
			500	-0.16	
SFM-BZY	BZY	NiO-BZY	650	-0.31	Lei et al,

					2017[20]
			600	-0.21	
			600	-0.10	
SLF	BZCY	NiO-BZCY	700	-1.08	Huan et al, 2018[21]
			650	-0.75	
			600	-0.46	
LSCF-BZY	BZY	NiO-BZY	700	-0.72	Bi et al, 2015[22]
			650	-0.39	
			600	-0.16	

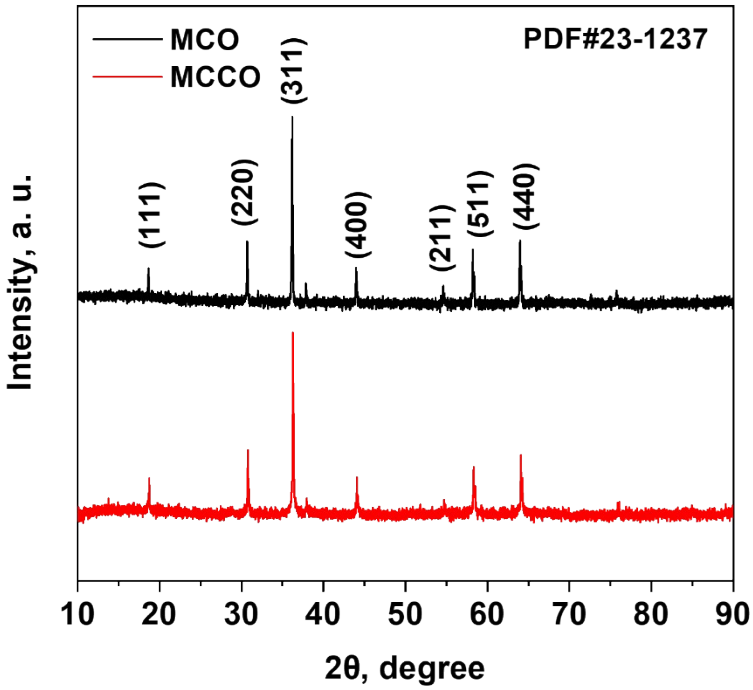

Figure S1. Typical XRD patterns of as-synthesized MCO and MCCO powder.

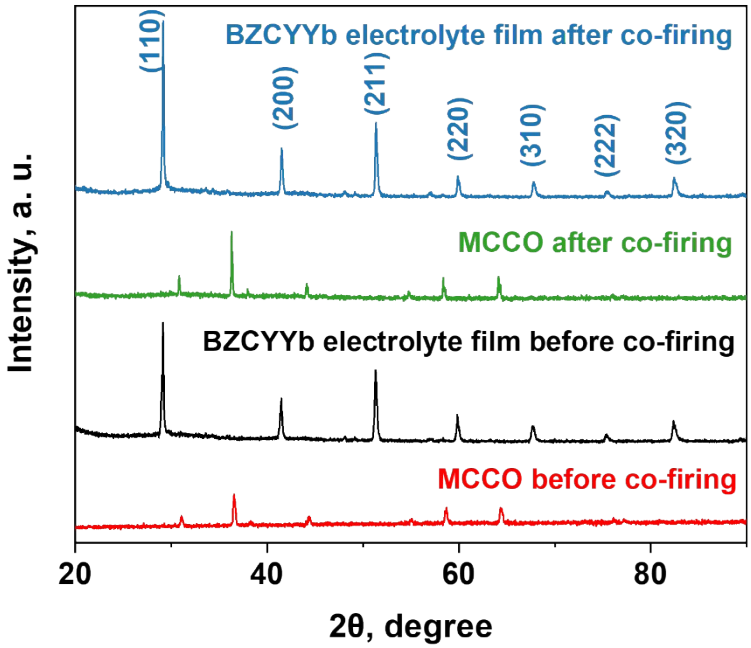

Figure S2. XRD patterns of BZCYYb and MCCO powder before and after co-firing at 900 °C for 10 min in air.

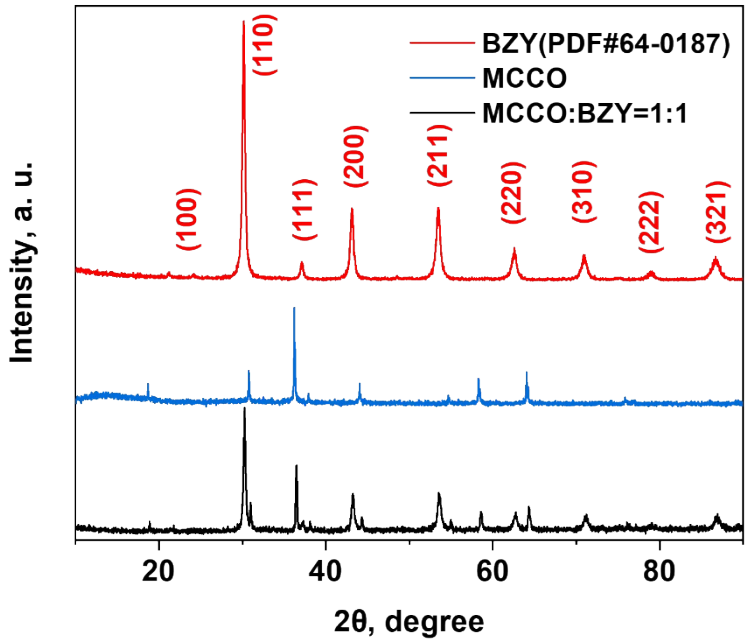

Figure S3. XRD patterns of BZY, MCCO, and MCCO-BZY powder after being fired at 900 °C for 10 min in air.

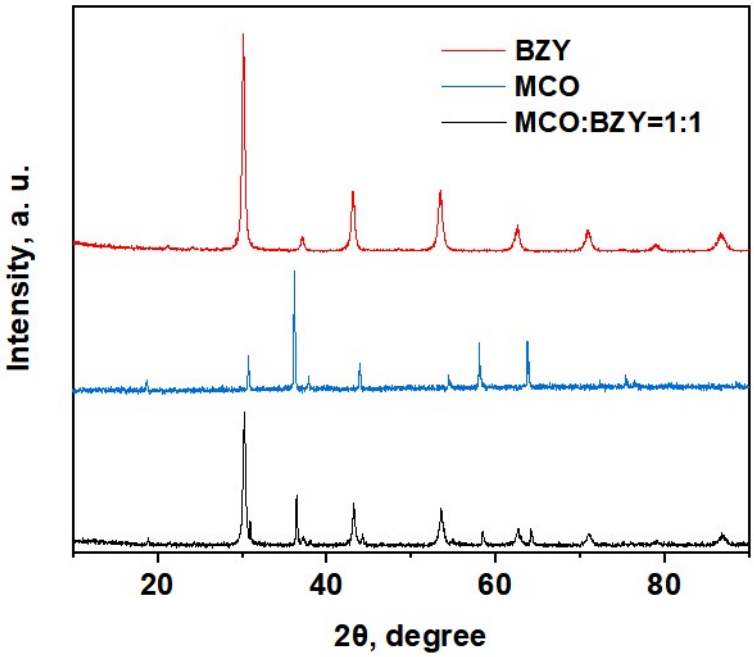

Figure S4. XRD patterns of BZY, MCO, and MCO-BZY powder after being fired at 900 °C for 10 min in air.

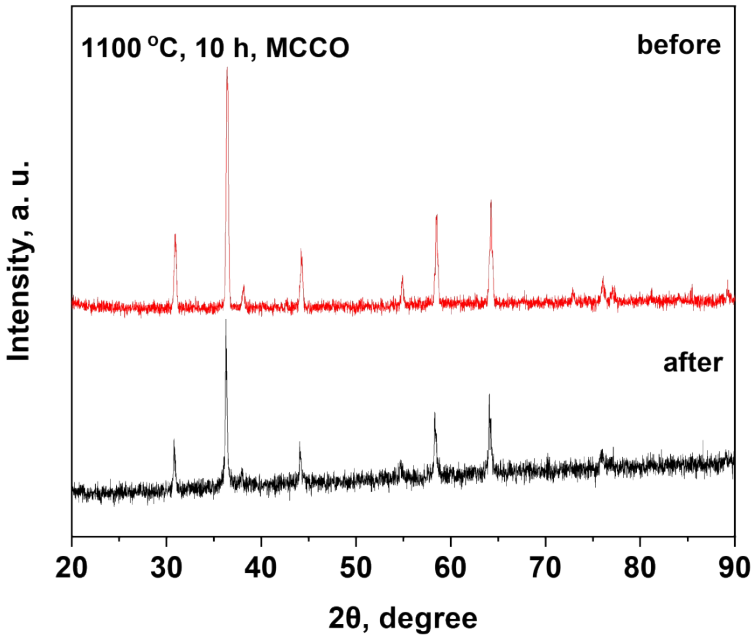

Figure S5. XRD pattern of the MCCO before and after being fired at 1100 °C for 10 h in air

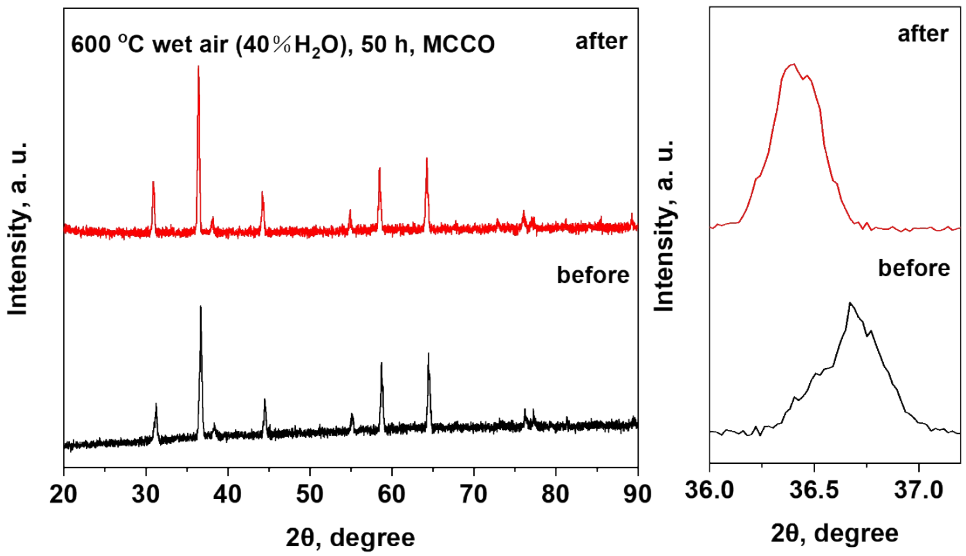

Figure S6. XRD patterns of MCCO powder before and after the treatment in wet air (40% H_2O) for 50 h at 600 °C.

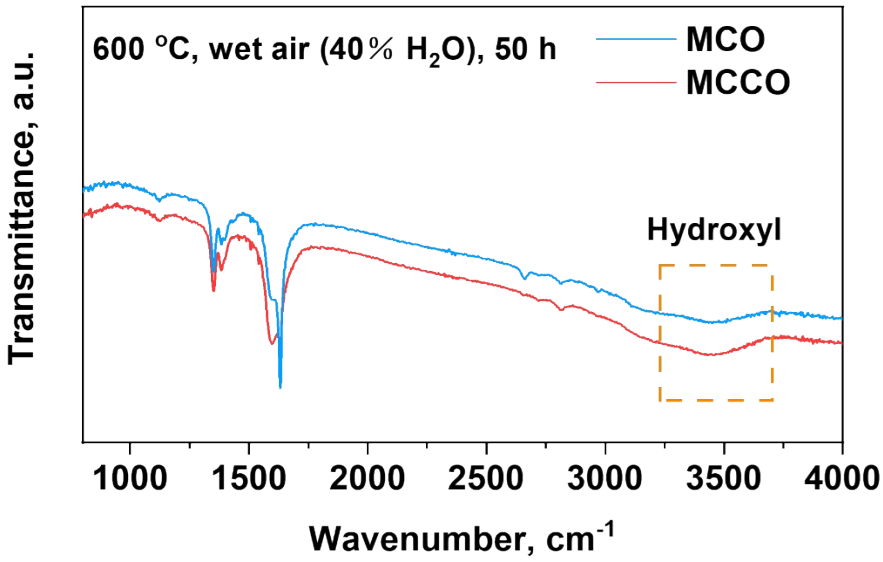

Figure S7. FTIR of MCO and MCCO powder after the treatment in wet air (40% H_2O) for 50 h at 600 °C.

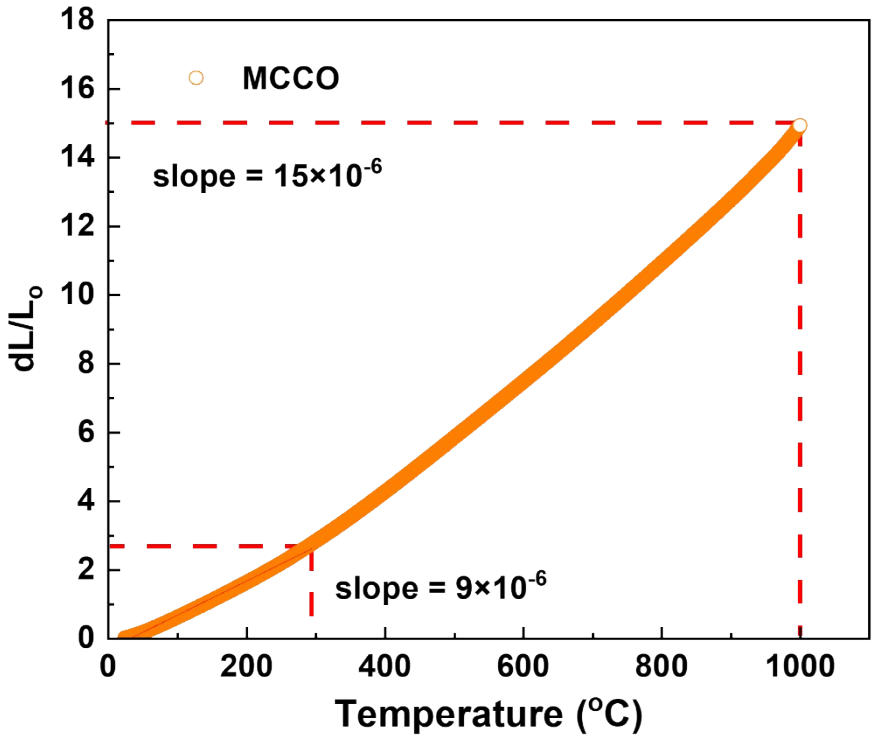

Figure S8. Thermal expansion behaviors of MCCO as a function of temperature (tested from RT to 1000 °C).

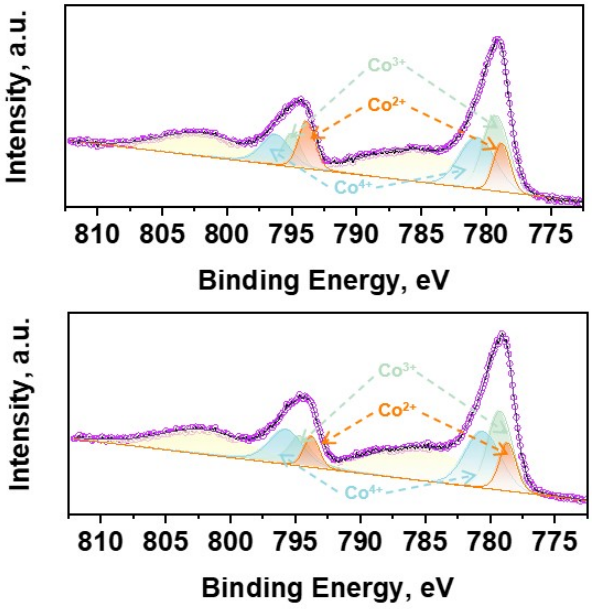

Figure S9. XPS spectra of Co $2p_{3/2}$ for MCO and MCCO powders.

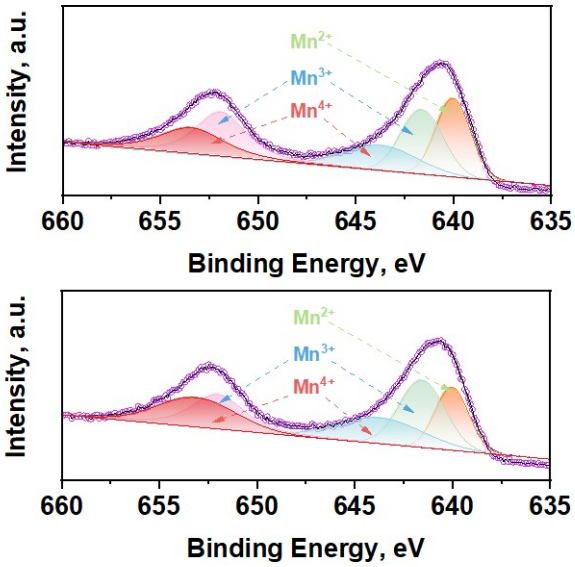

Figure S10. XPS spectra of Mn 2p for MCO and MCCO powder.

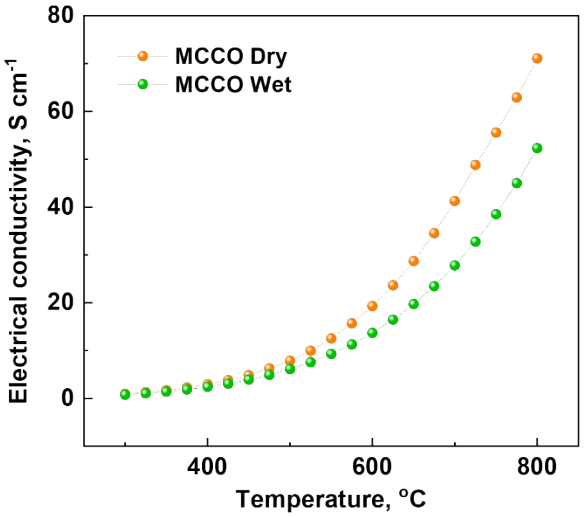

Figure S11. Electrical conductivity of MCCO in dry and wet air (3% H_2O)

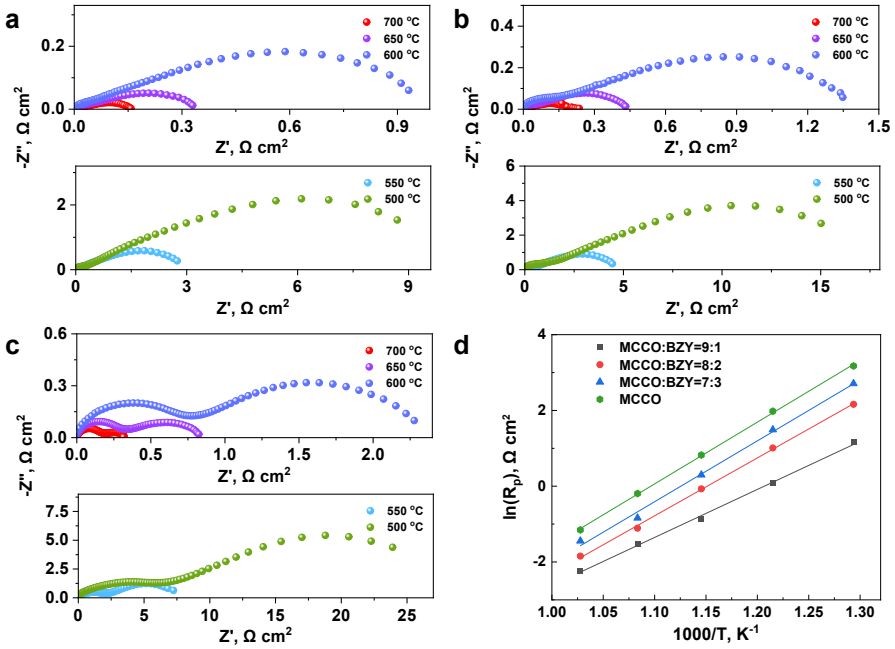

Figure S12. EIS of symmetrical cells with different MCCO-BZY mass ratios of a) 8:2, b) 7:3, c) EIS of symmetric cells with MCCO. d) R_p of symmetrical cells with composite electrodes with different proportions.

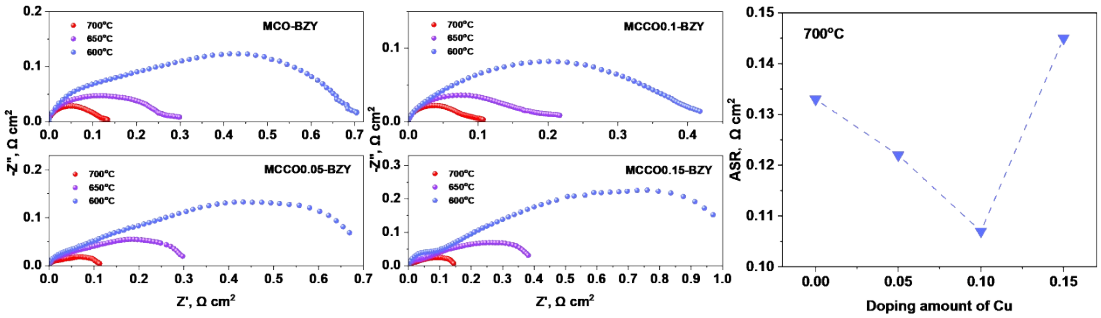

Figure S13. EIS of symmetrical cells with MCO-BZY, MCCO0.05-BZY, MCCO0.1-BZY, and MCCO0.15-BZY, and R_p of symmetrical cells with composite electrodes at 700 °C.

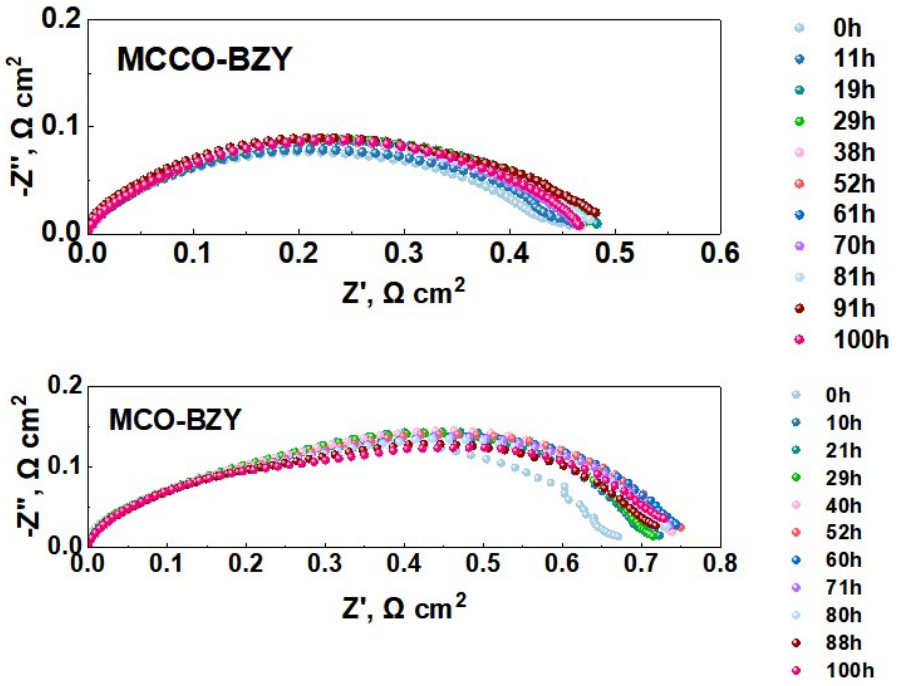

Figure S14. EIS of symmetrical cells measured in wet air at 600°C with MCCO-BZY electrode and MCO-BZY electrode under OCV condition for 100 h.

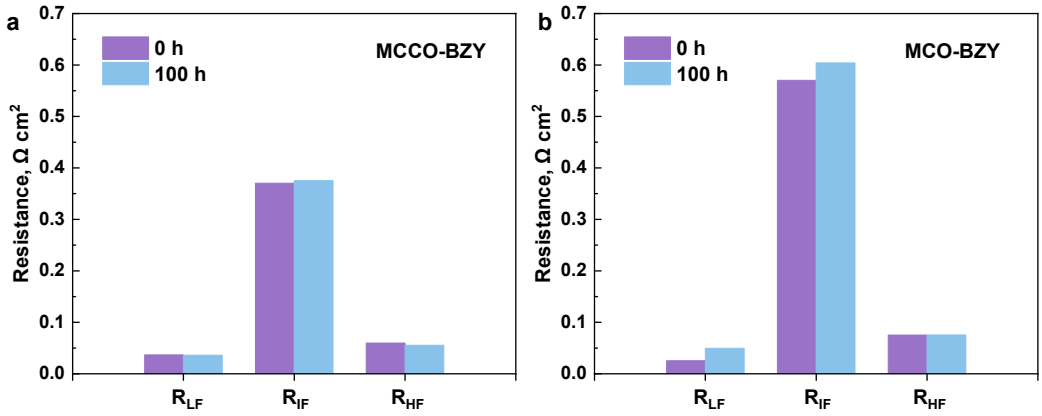

Figure S15. Comparisons of R_p of a) the MCCO-BZY and b) MCO-BZY in different frequency ranges.

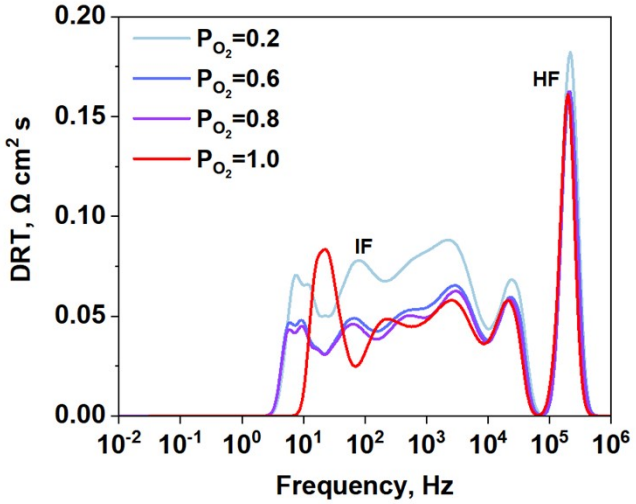

Figure S16. DRT analyses of R_p as a function of p_{O2} measured at 600°C

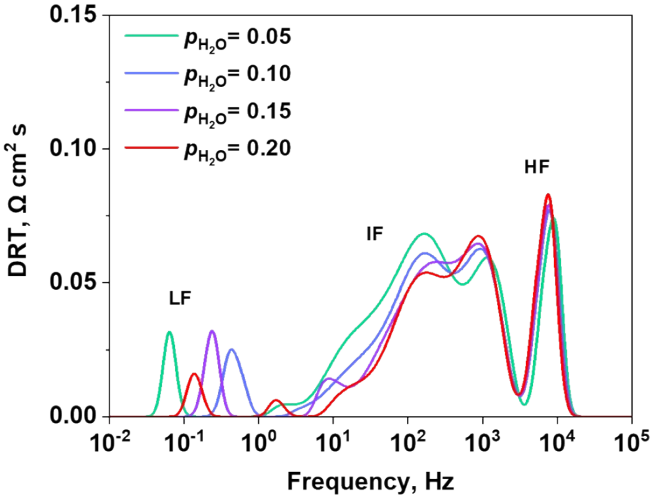

Figure S17. DRT analyses of R_p as a function of p_{H2O} measured at 600 °C

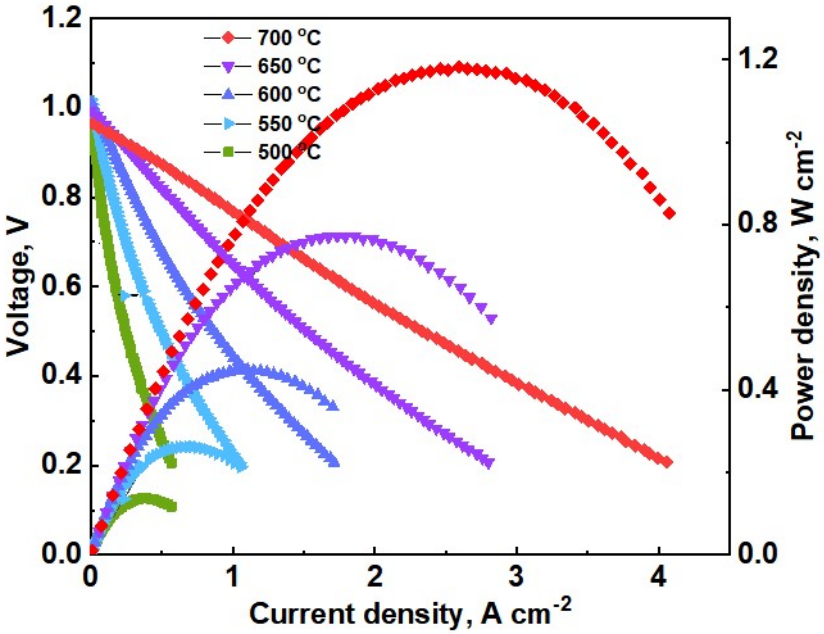

Figure S18. I-V-P curves of single cells with MCO-BZY electrodes measured at 500-700 °C in FC mode.

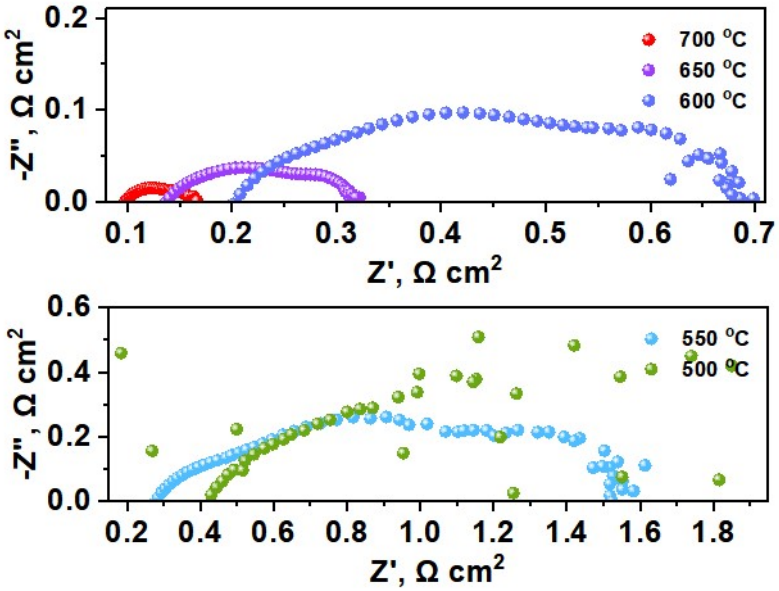

Figure S19. EIS curves of the single cells measured at OCV conditions with MCO-BZY.

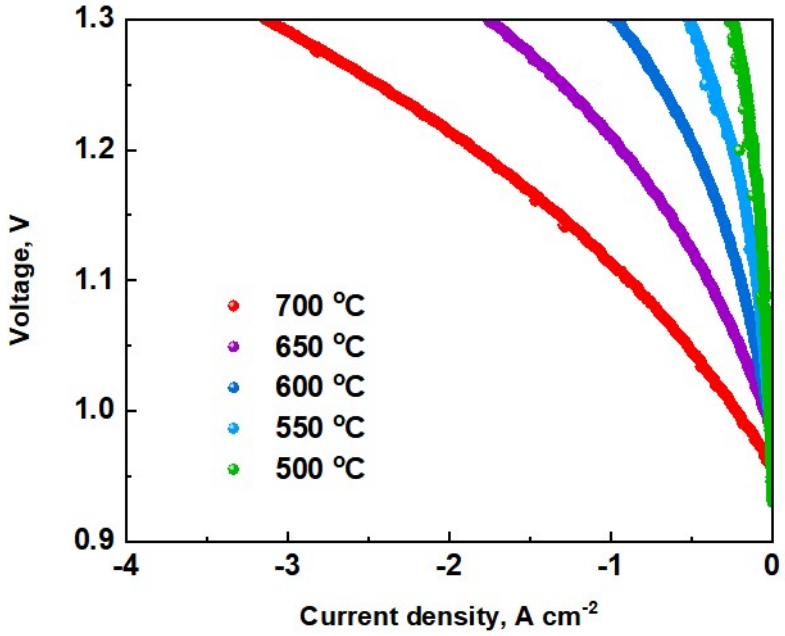

Figure S20. I-V curves of single cells with MCO-BZY electrodes measured at 500-700 °C in EL mode.

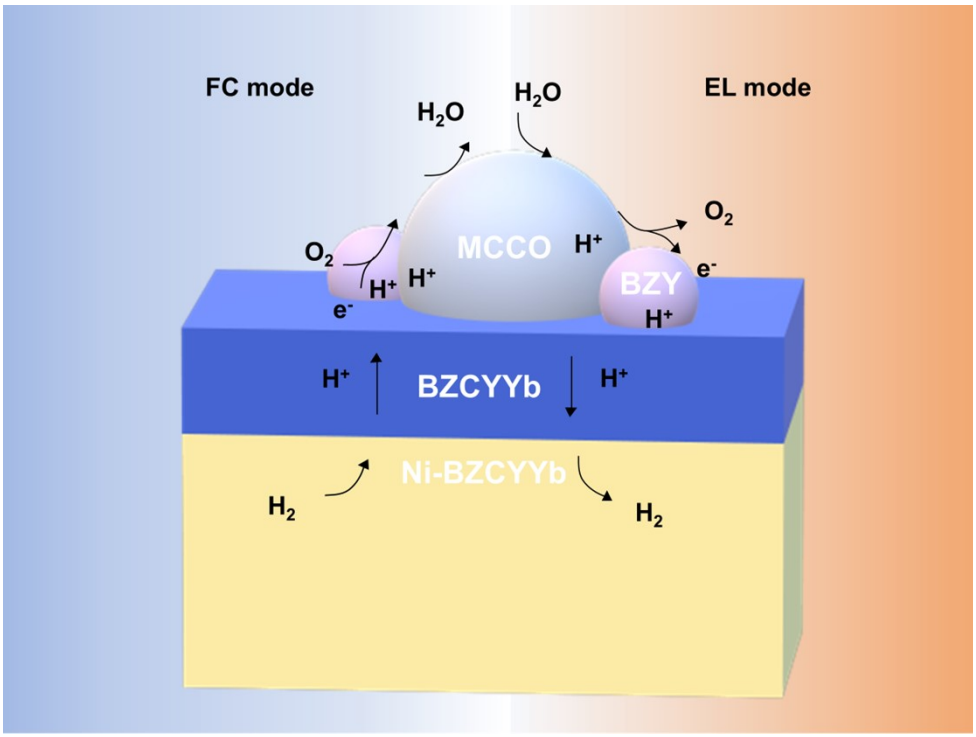

Figure S21. Schematic illustration of an R-PCEC operated in both fuel cell and electrolysis modes

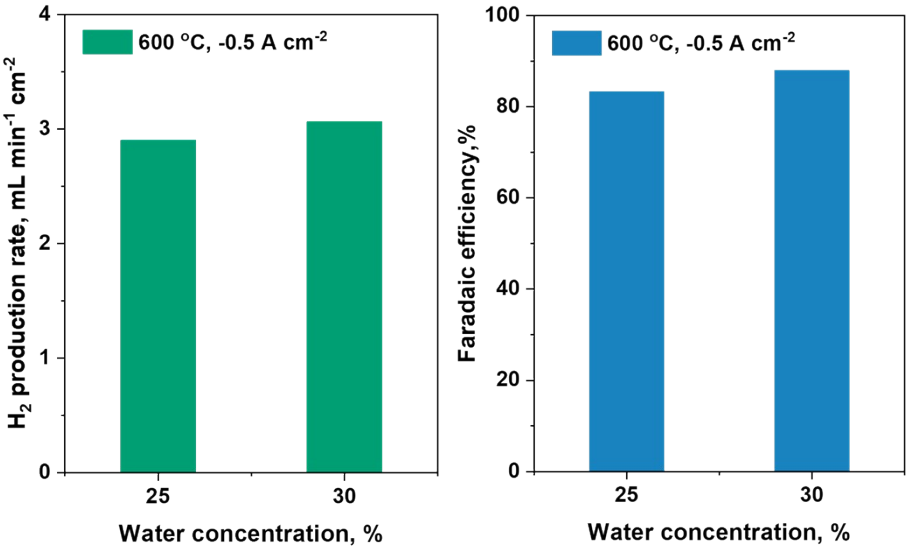

Figure S22. Faradaic efficiency at -0.5 A cm^{-2} in wet air with 25 and 30 vol.% H_2O at 600 °C.

References

1. Y. Yamazaki, R. Hernandez-Sanchez and S.M. Haile, *Chem. Mat.*, 2009, **21**, 2755-2762.
2. D.L. Han and T. Uda, *J. Mater. Chem. A*, 2018, **6**, 18571-18582.
3. F. He, S. Liu, T. Wu, M.T. Yang, W.H. Li, G.M. Yang, F. Zhu, H. Zhang, K. Pei, Y. Chen, W. Zhou and Z.P. Shao, *Adv. Funct. Mater.*, 2022, **32**, 10.
4. Z. Wang, P.F. Lv, L. Yang, R. Guan, J.D. Jiang, F.J. Jin and T.M. He, *Ceram. Int.*, 2020, **46**, 18216-18223.
5. Z.X. Yu, L. Ge, Q. Ni, Y.F. Zheng, H. Chen, X.K. Zhou, Y.W. Mi, B.C. Shi, X.L. Yu, B.Z. Wu, L. Bi and Y.F. Zhu, *Adv. Funct. Mater.*, 2024, **34**, 10.
6. I. Thaheem, K.J. Kim, J.J. Lee, D.W. Joh, I. Jeong and K.T. Lee, *J. Mater. Chem. A*, 2019, **7**, 19696-19703.
7. N. Li, L.P. Sun, Q. Li, T. Xia, L.H. Huo and H. Zhao, *J. Power Sources*, 2021, **511**, 8.
8. S.Y. Zhen, W. Sun, P.Q. Li, G.Z. Tang, D. Rooney, K.N. Sun and X.X. Ma, *J. Power Sources*, 2016, **315**, 140-144.
9. H.Y. Liu, X.F. Zhu, M.J. Cheng, Y. Cong and W.S. Yang, *Int. J. Hydrog. Energy*, 2013, **38**, 1052-1057.
10. Y.Y. Rao, Z.B. Wang, L. Chen, R.F. Wu, R.R. Peng and Y.L. Lu, *Int. J. Hydrog. Energy*, 2013, **38**, 14329-14336.
11. J.H. Cui, Y.H. Gong, R.Z. Shao, S.S. Wang, J.L. Mao, M. Yang, W.F. Wang and Q.J. Zhou, *J. Mater. Sci.-Mater. Electron.*, 2019, **30**, 5573-5579.
12. H.Y. Liu, X.F. Zhu, M.J. Cheng, Y. Cong and W.S. Yang, *Chem. Commun.*, 2011, **47**, 2378-2380.
13. L. Shao, Q. Wang, L.S. Fan, P.X. Wang, N.Q. Zhang and K.N. Sun, *Chem. Commun.*, 2016, **52**, 8615-8618.
14. Y.S. Xu, X. Xu and L. Bi, *J. Adv. Ceram.*, 2022, **11**, 794-804.
15. Y.S. Xu, Y.Y. Gu and L. Bi, *J. Mater. Chem. A*, 2022, **10**, 25437-25445.
16. X. Yang, Y.S. Xu, S.F. Yu and L. Bi, *Ceram. Int.*, 2022, **48**, 34098-34104.
17. J. Kim, A. Jun, O. Gwon, S. Yoo, M. Liu, J. Shin, T.H. Lim and G. Kim, *Nano Energy*, 2018, **44**, 121-126.
18. S.J. Yang, Y.B. Wen, J.C. Zhang, Y. Lu, X.F. Ye and Z.Y. Wen, *Electrochim. Acta*, 2018, **267**, 269-277.
19. W. Tang, H.P. Ding, W.J. Bian, W. Wu, W.Y. Li, X.B. Liu, J.Y. Gomez, C.Y.R. Vera, M. Zhou and D. Ding, *J. Mater. Chem. A*, 2020, **8**, 14600-14608.
20. L.B. Lei, Z.T. Tao, X.M. Wang, J.P. Lemmon and F.L. Chen, *J. Mater. Chem. A*, 2017, **5**, 22945-22951.
21. D.M. Huan, W.H. Wang, Y. Xie, N. Shi, Y.H. Wan, C.R. Xia, R.R. Peng and Y.L. Lu, *J. Mater. Chem. A*, 2018, **6**, 18508-18517.
22. L. Bi, S.P. Shafi and E. Traversa, *J. Mater. Chem. A*, 2015, **3**, 5815-5819.